Proceedings of the Canadian Society for Mechanical Engineering International Congress
32nd Annual Conference of the Computational Fluid Dynamics Society of Canada
Canadian Society of Rheology Symposium
CSME/CFDSC/CSR 2025
May 25–28, 2025, Montréal, Québec, Canada

NUMBER

Evolution of wall pressure and wall shear stress under adverse pressure gradients from attached to separated flows

Arnaud Le Floc'h[1*], Nan Hu[1], Alexandre Suryadi[1], Michaela Herr[1]

[1]Department of Wind Energy, Institute of Aerodynamics and Flow Technology, Deutsches Zentrum für Luft und Raumfahrt (DLR)
Lilienthalplatz 7 38108 Braunschweig, Germany
[*]arnaud.lefloch@dlr.de

March 28, 2025

***Abstract*—**We present a new database of wall pressure and shear stress for a family of turbulent flows under strong adverse pressure gradients (APG). We aim to predict the attached or separated state of the flow based on wall quantities and new perspectives are discussed in the present study.

***Keywords-component*—flow separation; wall pressure fluctuations; wall shear stress; oil film visualizations**

I. Flow separation challenges for Wind Energy

At high angles of attack (AoA), the boundary layer near the trailing edge of a wind turbine blade can experience flow separation, leading to detrimental performances for the wind park and an increase in noise emission [1]. The complex unsteady nature of separated flows remains an active field of research, as the mechanisms driving the wall-pressure response are still poorly understood. However, long-term objectives for wind energy at DLR include improved prediction of such adverse conditions with the use of on-board sensors and AI-led real-time monitoring. In an effort to pursue that goal, a recent study investigated the similarities of wall pressure signatures between separated flows on a flat plate versus near the trailing edge of two distinct airfoils [2].

Of particular interest, the onset of separation (upstream of the mean detachment) presented unique characteristics that included a positive skewness and strong low-frequency activity in wall pressure linked to the so-called breathing cycles of the recirculation region. However, to date, the relevance of the breathing motion to noise emissions is still being debated in spite of being the dominant contributor to turbulent kinetic energy for separated flows. Moreover, it was also observed in [2] that each dataset suffered from limitations that prevented acquiring the full range of frequencies associated with flow separation, ranging from the low- frequency breathing up to small scales of backflow. Our objective in this paper is to cover low-, mid-, and high-frequency activities using comprehensive instrumentation to yield a novel database with full spectral resolution that AI algorithms can later use for training.

II. A new ZPG-APG flow database at DLR

A. Experimental setup in the AWB wind tunnel

In order to overcome the aforementioned limitations, the present study investigates comprehensive surface measurements in a pressure-induced flow separation test campaign on a flat plate, following the work of Hu (2018) [3]. A flat wooden plate is installed 10 mm downstream of a rectangular nozzle that is 1.2 m high per 0.8 m wide and the plate is fixed in a horizontal plane parallel to the mean flow direction as shown in Fig. 1.

As Hu (2018) previously documented, the wind tunnel background noise is significant in the frequency range of $f < 300$ Hz, where the signal-to-noise ratio was considered to make it impossible to capture turbulent instability. An effort was made to combine different wall pressure sensors to respond to that problem: an array of ten Kulite sensors, including seven in the streamwise direction as well as seven GRAS sensors. A novel design for the experiment was to insert three pairs of GRAS microphones and IC2 wall shear stress sensors to investigate the relationship (p, τ)), and validate

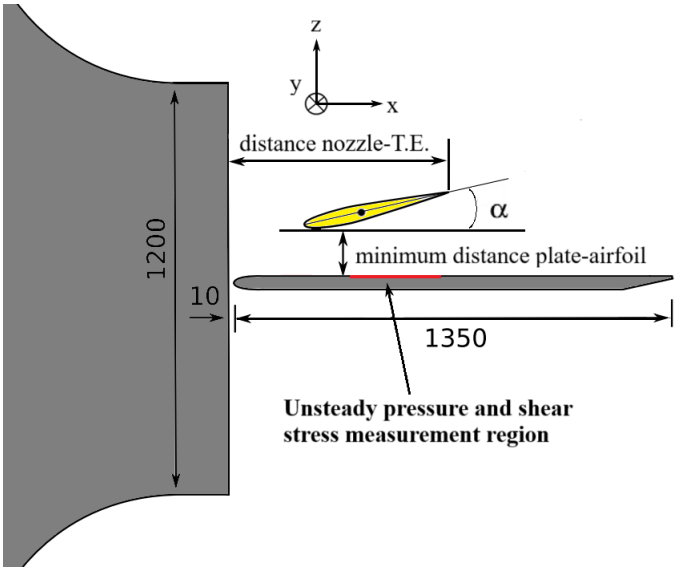

Figure. 1. Side view schematics of the test section. Dimensions are in mm.

the existence of mean backflow in certain cases. Indeed, synchronized measurements of wall shear stress are performed as well using IC2 shear stress capacitive sensors to further document the link between wall-pressure and wall-shear.

We summarize in Table 1 the locations for the IC2 wall shear stress sensors, the Kulite sensors as well as the GRAS microphones that were used in the experiment. Note that different techniques of mounting were applied to install our instrumentation, with the use of pinholes as small as 0.4 mm diameter for GRAS sensors. Each sensor has their own advantage: the main idea was that at the onset of separation, we want to resolve the low-frequency as well as the convection motion inside the expected recirculation bubble where GRAS can efficiently be used. At higher frequencies, Kulite sensors are also used to detect backflow motion in addition to the regular vortex shedding as described in [2]. All these sensors in the present study are then inserted in a 370 mm by 270 mm aluminum panel that also includes wall static pressure ports and is flush-mounted to the wooden plate. Note that the reference position corresponds to $x = 770$ mm and Kulite n°4, GRAS n°2 and the IC2 shear stress n°2 are all located at the streamwise origin.

B. Towards the creation of different APG intensities

Moreover, a diverse range of pressure gradients is created by installing a two-dimensional movable extruded profile NACA-0012 with a chord length of 400mm and its angle of attack (AoA) can be changed thanks to a rotation axis defined at 41% of the chord. After investigating three AoAs ($14.8°$, $12.2°$ and $10.0°$), we selected five streamwise positions for the NACA 0012 to cover the onset, the middle, and the end region of flow separation. The following distances nozzle to trailing edge are $X0 = 660$ mm, $X1 = 700$ mm, $X2 = 785$ mm, $X3 = 870$ mm and $X4 = 990$ mm.

TABLE. I
LIST OF SENSORS

Sensor Positions:	**Reference (0,0) is the Kulite 4 @ $x = 770$ mm**		**Surface mounting**
Name	x [mm]	y[mm]	
IC2 Shear stress n°1	-25	30	flush mounted
IC2 Shear stress n°2	0	30	flush mounted
GRAS n°1	-25	15	0.4 mm pinhole
GRAS n°2	0	15	0.4 mm pinhole
GRAS n°3	35	15	0.4 mm pinhole
GRAS n°4	20	30	0.4 mm pinhole
GRAS n°5	0	-15	flush mounted
GRAS n°6	-430	-155	Hard fairing (denoising n°1)
GRAS n°7	0	-155	Hard fairing (denoising n°2)
Kulite n°1	-65	0	0.5 mm pinhole
Kulite n°2	-25	0	0.5 mm pinhole
Kulite n°3	-5	0	0.5 mm pinhole
Kulite n°4	**0**	**0**	0.5 mm pinhole
Kulite n°5	2	0	0.5 mm pinhole
Kulite n°6	12	0	0.5 mm pinhole
Kulite n°7	40	0	0.35 mm pinhole
Kulite n°8	0	2	0.7 mm pinhole
Kulite n°9	0	-4	flush mounted with screen
Kulite n°10	0	9	flush mounted with no screen

III. EXPERIMENTAL RESULTS

A. Mean flow topologies

Fig. 2 shows the oil film visualizations that were obtained for an AoA of $12.2°$ and with a reference inlet velocity $U = 30$ m/s. The flow conditions we could generate included a canonical ZPG turbulent boundary layer, followed by a mild APG case, a normal case, and then strong and very strong ones, leading to finally the occurrence of mean backflow on the plate. Both sides of the airfoil were tripped around 10% of the chord with a zigzag strip and vortex generators were also taped on the pressure side. Wool tuft visualizations (not shown for brevity) indicated that the vortex generators enabled the flow to remain attached on the airfoil for the three considered AoAs, but could separate on the flat plate. Note that beyond $15°$, the flow started to visibly separate on the NACA profile.

We gather in Table 2 the results of different flow topologies that we obtained and three categories can be observed. The first one shows the ZPG and mild APG cases ($z = 110 - 90$ mm), where the flow is consistently flushed downstream, and the secondary flow formed by the shear layers at the nozzle side walls tends to slowly "pinch" the primary flow region in the aft region. The second category is composed of the **strong APG** flows ($z = 66 - 51$ mm) and we can now observe an oil accumulation in the region where the flow is strongly decelerated. The third and last category is for the actual flow separations ($z = 40 - 25$ mm) with formation of a typical "stall cell" with a saddle point flanked by two foci on the sides. These structures belong to the so-called owl face patterns of

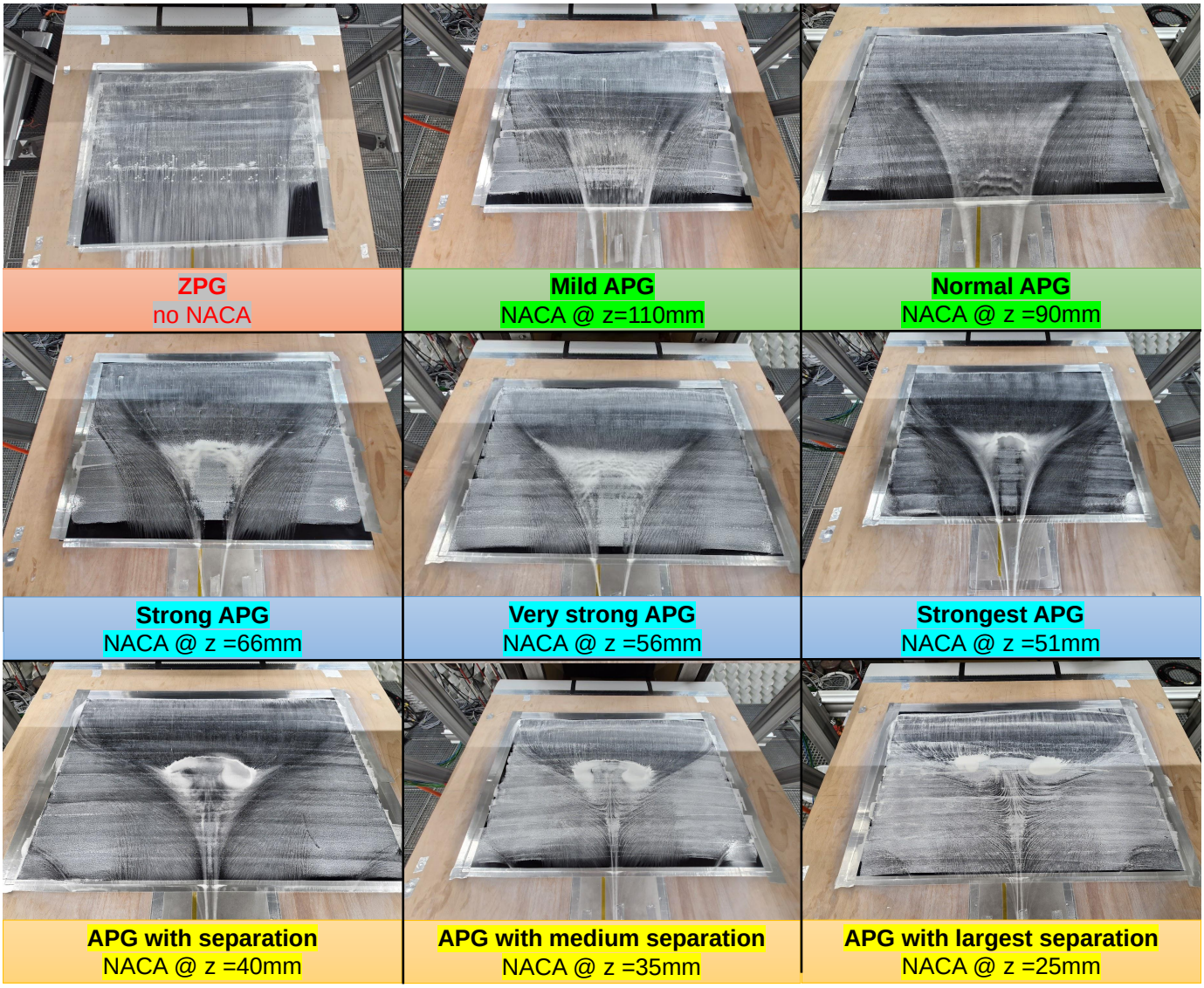

Figure. 2. Oil film visualizations for ZPG and with APG conditions.

TABLE. II
FLOW RESULTS TOPOLOGIES OBTAINED FOR MULTIPLE DEPTHS Z

	Minimum distance plate-airfoil [mm]	Comments
Z1	25	Separation (stall cell)
Z2	35	Separation (stall cell)
Z3	40	Separation (stall cell)
Z4	66	Strong APG (no separation)
Z5	56	Very strong APG (no separation)
Z6	51	Strongest APG (no separation)
Z7	45	Strongest APG no/or small separation
Z8	90	Normal APG (no separation)
Z9	110	Mild APG (no separation)
Z10	130	Weakest APG (no separation)

the first kind, consisting of a single saddle point at separation and reattachment [5].

B. Mean wall pressure and shear stress distributions for different APG conditions

We first present the main features of the turbulent boundary layers that we analyzed. Compared to the Schlichting ZPG law ($c_f/2 = 0.0128 Re_\theta^{-0.25}$), Table 3 presents our canonical ZPG results that are slightly smaller, as well as the rest of our APG cases. The Reynolds numbers, based on the frictional quantity and the momentum thickness, cover a progressive range of decelerated flow conditions using a 1D hot wire anemometer. Finally, note that the values from Table 3 were all derived from the streamwise reference location at $x = 770$ mm.

We now move on to the analysis on both mean wall pressure and shear stress distributions for the corresponding cases described in Fig. 2. The progressive evolution from ZPG to APG flow conditions is shown in Fig. 3, the NACA profile was set at the streamwise position $X3$. The decrease in the pressure coefficient reflects the airfoil moving gradually closer

TABLE. III
TURBULENT BOUNDARY LAYER PARAMETERS FOR MULTIPLE DEPTHS Z

Flow conditions	U_∞ **[m/s]**	U_e**[m/s]**	δ**[mm]**	δ^***[mm]**	θ**[mm]**	$H = \delta/\theta$	u_τ**[m/s]**	Re_τ	Re_θ
ZPG	30	28.6	12.6	2.19	1.56	1.41	1.197	1004	2965
Weakest APG – NACA@X3,Z10	30	29.8	15.2	3.33	2.16	1.54	1.057	1067	4286
Mild APG – NACA@X3,Z9	30	30.6	16	3.89	2.4	1.62	1.001	1070	4907
Normal APG –NACA@X3,Z8	30	30.2	17.1	4.56	2.66	1.71	0.907	1032	5348
Strong APG – NACA@X3,Z4	30	29.5	18.7	6.19	3	2.06	0.652	808	5855
Very strong APG – NACA@X3,Z5	30	29.1	21.2	8.12	3.47	2.34	0.488	684	6679
Strongest APG –NACA@X3,Z6	30	28.1	22.7	10.3	3.46	2.98	0.293	435	6361

to the flat plate. Note that the ZPG is already slightly in weak APG condition, as previously documented in [3].

Consistently with the oil film visualizations in Fig. 2, the DC values for the shear stress sensors were negative for the four closest z heights of the NACA profile, in which $z = 45$ mm also showed a negative shear value. Indeed, the oil accumulation was already quite visible at $z = 51$ mm, but the visualization at $z = 45$ mm could not be done. The subsequent two subplots in Fig. 3 deal with the complete distribution for c_p and τ_w for the first three heights ($z1$, $z2$ and $z3$ with separation). The effect of increasing the AoA (from $10.0°$ to $12.2°$) is seen in the amplitude of decrease in the c_p coefficient, as the separation is stronger with an increased AoA. Secondly, the minimum height z has a clear impact on the magnitude of the wall pressure gradient that we imposed. The corresponding mean wall shear stress values are displayed in Fig. 3 as well. In spite of a certain drift of the DC component that was observed, we could compute a meaningful trend of the shear stress for these two AoAs. The separation region appears to shift in the upstream direction when we moved the NACA closer to the flat plate, especially so for $z1$. Such observations appear consistent with the oil film visualizations where the saddle point for the $z1$ case appears visibly at a more upstream position than $z2$, and even more so than $z3$. The turbulent separation bubble is therefore located a bit more downstream with increasing height of the NACA profile.

C. Low-, mid- and high- frequency spectral response

In this section, we focus on the spectral content of both pressure and shear for the case of the height $z2 = 35$ mm. Following [2], the merge of different databases between flat plate and airfoil measurements revealed promising features to detect and classify flow separation. Both sides of the spectrum are now investigated as we want to identify the entire unsteady portrait of our TSB. First, the Kulite spectral response is shown on top of Fig. 4. Ranging from upstream positions (curves in blue) to downstream ones (curves in red), the streamwise locations going from $x = 435$ mm to $x = 810$ mm are the same as in Fig. 3 to ease the comparison. Several remarkable features can be highlighted from these results: first, the pinhole inserts that were used allowed for a resonance peak that was pushed as far as possible in the high frequency ranges between $[1 - 2] * 10^4$ Hz, enabling a proper investigation at high frequency including for the convective motions. As it happens, a global peak forms gradually when

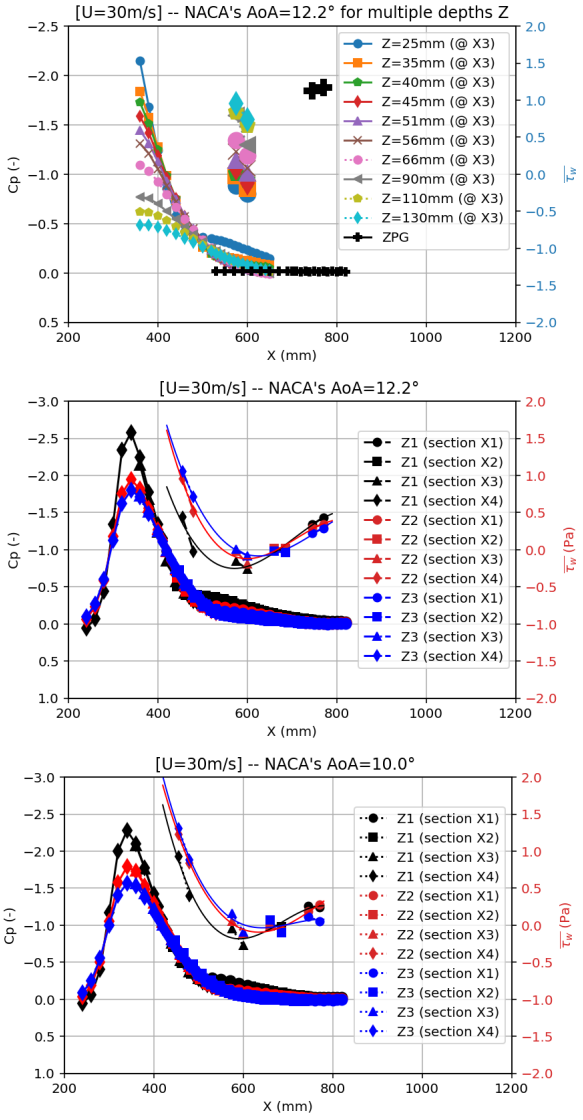

Figure. 3. Streamwise distribution of mean wall pressure and wall shear stress with $U = 30$ m/s. Top: Evolution for multiple z heights. Middle: Complete distribution for NACA $AoA = 12.2°$. Bottom: Complete distribution for NACA $AoA = 10.0°$.

moving downstream, starting near the onset of separation near $x \simeq 470$ mm and becomes dominant in the separated region around $f = 110$ Hz. When scaling with the length of mean backflow, such frequency gives a Strouhal number: $St_{Lsep} = fL_{sep}/U \simeq= 0.66$. This result matches the typical signature of the classical vortex shedding, due to the Kelvin-Helmholtz instability in the separated shear layer. Finally, the Kulite sensors depict the same combination of a dual slope in the streamwise range of $x = 600 - 700$, where Le Floc'h et al. [2] illustrated the superposition of a dual convective motion, composed of the classical vortex shedding running downstream and the convected motion of small scale structures in the backflow region going in the opposite direction.

Subsequently, similar conclusions can be drawn from the GRAS spectra, presented in the middle of Fig. 4. Note that the streamwise distribution for the GRAS is sparser than for Kulite's, but the color code was left unchanged. Amplitudes in the high frequency range 10^4 Hz appear clearly attenuated compared to Kulite's results, which was expected per design of the sensors [3]. Nonetheless, GRAS sensors can properly capture the low frequency part of the spectrum ($f < 100$ Hz), and the results interestingly show, especially for the upstream region (cf. blue curves $x = 455 - 515$ mm), that two peaks in the range $f < 100$ Hz can clearly be identified. At this point, the question arises whether such peaks are physical, or due to the noise pollution from the wind tunnel and/or the shear layers emanating from the nozzle side walls.

Before tackling the issue of de-noising our Power Spectral Densities (PSD) in the next section, we wrap up the spectral analysis of our TSB at $z = z2$ with the shear stress response. Indeed, the pair of IC2 shear stress sensors located at $x = 745$ mm (next to GRAS $n°1$) and $x = 770$ mm (next to GRAS $n°2$) were synchronously recorded and their PSDs are presented at the bottom of Fig. 4. Due to a mass-spring resonance of the floating element [6], a resonance peak is visible at 2.5 kHz. Once again, the color code used in the figure are the same as for the pressure sensors, and additional information can be extracted from the spectra. First, the upstream of the bubble and reattachment region (blue and red curves, respectively) show higher amplitudes than the green and yellow curves corresponding to the separation region. This observation is consistent with Fig. 3 where the DC component recorded by the IC2 sensors showed a significant decrease in wall shear in the recirculation before increasing again after reattachment. Similar to [7], a low frequency peak is not really visible in spite of high amplitudes, whereas the occurrence of the vortex shedding is associated with a clear and much faster roll-off for the range $f > 100$ Hz for the convective motion.

D. Noise filtering

In our last section, we focus on the issue of the noise polluting our spectral results. Indeed, the AWB wind tunnel background noise is known to be significant for the low frequency range [3], hence the need to properly account for it in our PSDs. In an effort to implement a correction, GRAS

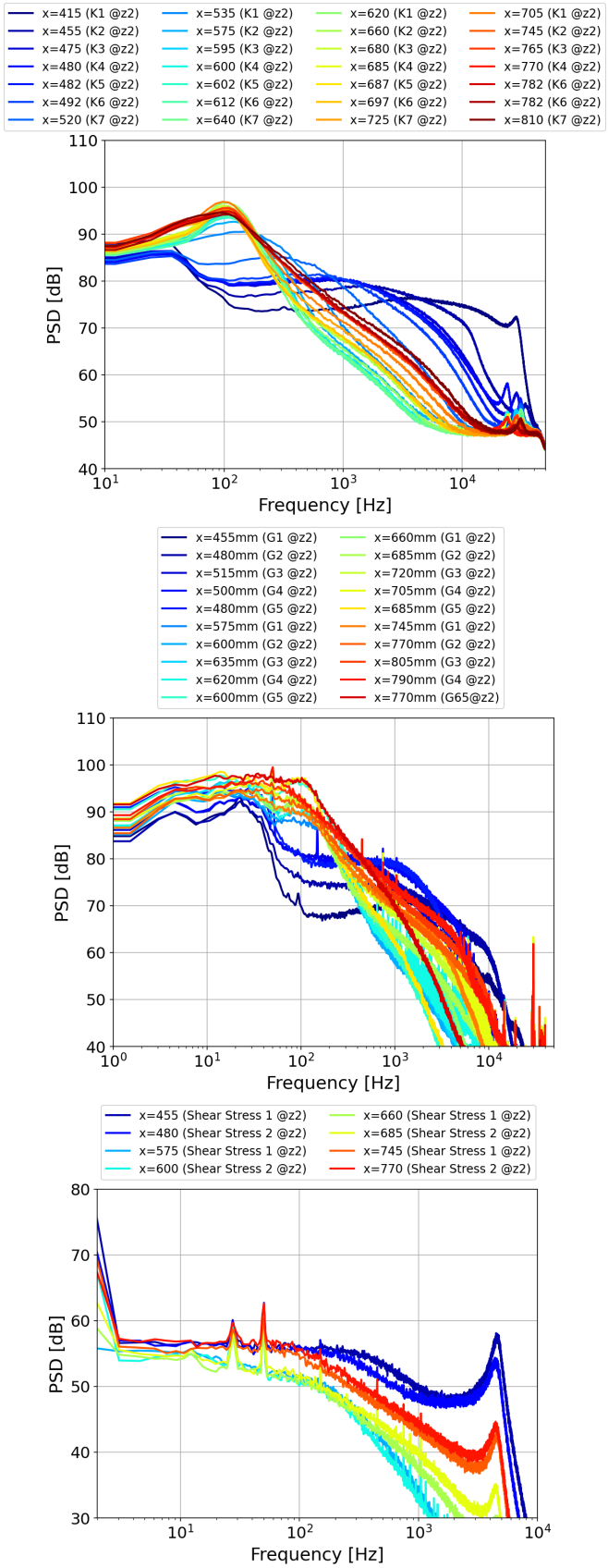

Figure. 4. Top: Kulite PSDs @$z2 = 35$ mm. Middle: GRAS PSDs @$z2 = 35$ mm. Bottom: IC2 shear stress PSDs @$z2 = 35$ mm.

sensors $n°6$ ($G6$) and $n°7$ ($G7$) were placed away from the measurements region with $G6$ located far upstream and $G7$ to the right side (negative y axis). To remove the noise component in our spectra, the following subtraction technique from [4] is used to get the PSD G_{nn}, using the corrected G_{yy} with the help of a secondary sensor G_{xx} located away from G_{yy}:

$$G_{nn}(f) = [1 - C_{xy}(f)]G_{yy}(f) \quad (1)$$

The impact of the shear layer is expected to be visible in the $f < 100$ Hz and comes as a limitation of the quasi-2D flow region we can consider on the flat plate. In the top of Fig. 5, we show the results of the square magnitude coherence between GRAS sensors $G1$ and the two reference ones $G6$ (Ref. 1) and $G7$ (Ref. 2). The correction was tested for three different configurations, with the ZPG configuration (curves in black), with a regular APG condition (curves in red at $z8 = 90$ mm) and finally with separated flow conditions (curves in blue at $z3 = 40$ mm). Remarkably, we observe that both reference GRAS exhibit a high level of coherence with GRAS $n°1$ located in the range $f < 10$ Hz. The coherence is maximum in the ZPG case, where there should be almost no low frequency activity, implying that both sensors ($G1$ and $G6-7$) face the same level of pollution coming from the wind tunnel, including the flapping shear layers coming out of the nozzle side walls. As the APG intensity increases, the energy shifts towards lower frequency ranges and the coherence levels are still significant, which is consistent with the literature [8]. Applying the correction to the GRAS spectra from Fig. 4, we now present the corrected PSDs at the onset of the TSB for three streamwise positions($x = 455$, 480 and 515 mm). Upstream of the mean detachment (located around $x \simeq 550$ mm), a peak at $f \simeq 15-20$ Hz is now appearing, giving a Strouhal number of $St_{Lsep} = fL_{sep}/U \simeq= 0.09 - 0.12$. This could be related to the breathing motion discussed in [2], and further work will focus on identifying such low-frequency motion.

IV. Conclusion

An experimental family of ZPG and APG flow conditions were investigated in the AWB wind tunnel. A new database was produced in order to obtain a progressive evolution of wall-pressure and wall-shear stress from attached to separated flows. The presence of a movable NACA-0012 profile over a flat plate allowed us to cover an elongated streamwise direction over the separated region. A comprehensive set of pressure transducers enabled us to resolve both low and high frequency ranges, and synchronously recorded the shear stress mean and fluctuating values. Oil film visualizations and wall quantities have shown a consistent portrait of such APG flows, with an emphasis on the low frequency unsteadiness. A noise pollution filtering technique was applied in the frequency domain and revealed promising results in order to resolve the breathing motion of a turbulent separation bubble in spite of known experimental limitations. Additional work, including machine learning training and monitoring, will be necessary to tackle the challenge of flow separation detection and mitigation in wind energy.

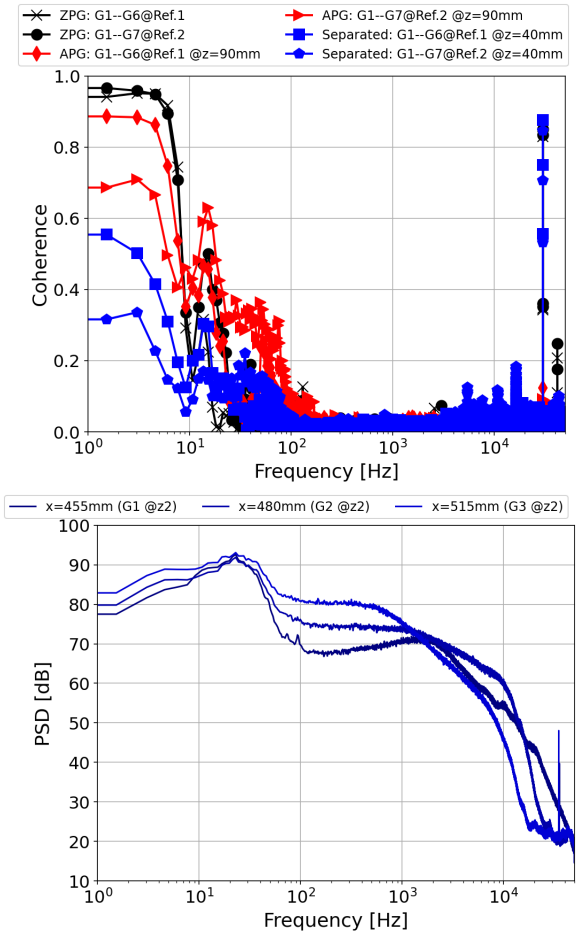

Figure. 5. Noise filtering in GRAS spectra. Top: Coherence between $G1$ and $G6-7$. Bottom: Corrected spectra at the onset of separation at $z = z2$.

Acknowledgment

This work is financed by DLR impulse project SAFER2.

References

[1] A. Suryadi , M. Herr. Wall pressure spectra on a DU96-W-180 profile from low to pre-stall angles of attack. In 21st AIAA/CEAS Aeroacoustics Conference, 2015.

[2] A. Le Floc'h, A. Suryadi, N. Hu, M. Herr, S. Wang, S. Ghaemi, G. Di Labbio, L. Dufresne, J. Vétel. Wall pressure signature of separated flows: A comparison between flat plate and airfoil, 2024.

[3] N. Hu (2018). Investigation of wall pressure fluctuations induced by turbulent boundary layer flow with pressure gradients (PhD thesis).

[4] J. S. Bendat and Allan G. Piersol. Random data: analysis and measurement procedures. John Wiley Sons, 2011.

[5] Simmons, D. J., F. O. Thomas, T. C. Corke,and F. Hussain. Experimental characterization of smooth body flow separation topography and topology on a two-dimensional geometry of finite span. Journal of fluid mechanics, 944, A42, 2022

[6] R. J. Pabon, L. Ukeiley, M. Sheplakand C. Barnard Keane. Characteristics of turbulent boundary layer large scale motions using direct fluctuating wall shear stress measurements. Physical Review Fluids, 2018.

[7] J. Weiss, B. Steinfurth, L. Chamard, A. Giani and P. Combette. Spectral proper orthogonal decomposition of unsteady wall shear stress under a turbulent separation bubble. AIAA Journal, 2022.

[8] J. Weiss, A. Mohammed-Taifour and Q. Schwaab. Unsteady behavior of a pressure-induced turbulent separation bubble. AIAA Journal, 2015.